



Dual optimization based prostate zonal segmentation in 3D MR images



Wu Qiu^{a,*}, Jing Yuan^a, Eranga Ukwatta^{a,b}, Yue Sun^{a,b}, Martin Rajchl^{a,b}, Aaron Fenster^{a,b,c}

^a Robarts Research Institute, University of Western Ontario, London, ON, Canada

^b Biomedical Engineering Graduate Program, University of Western Ontario, London, ON, Canada

^c Medical Biophysics, University of Western Ontario, London, ON, Canada

ARTICLE INFO

Article history:

Received 2 June 2013

Received in revised form 18 February 2014

Accepted 24 February 2014

Available online 4 March 2014

Keywords:

3D prostate MRI

Zonal segmentation

Convex optimization

Multi-region segmentation

ABSTRACT

Efficient and accurate segmentation of the prostate and two of its clinically meaningful sub-regions: the central gland (CG) and peripheral zone (PZ), from 3D MR images, is of great interest in image-guided prostate interventions and diagnosis of prostate cancer. In this work, a novel multi-region segmentation approach is proposed to simultaneously segment the prostate and its two major sub-regions from only a single 3D T2-weighted (T2w) MR image, which makes use of the prior spatial region consistency and incorporates a customized prostate appearance model into the segmentation task. The formulated challenging combinatorial optimization problem is solved by means of convex relaxation, for which a novel spatially continuous max-flow model is introduced as the dual optimization formulation to the studied convex relaxed optimization problem with region consistency constraints. The proposed continuous max-flow model derives an efficient duality-based algorithm that enjoys numerical advantages and can be easily implemented on GPUs. The proposed approach was validated using 18 3D prostate T2w MR images with a body-coil and 25 images with an endo-rectal coil. Experimental results demonstrate that the proposed method is capable of efficiently and accurately extracting both the prostate zones: CG and PZ, and the whole prostate gland from the input 3D prostate MR images, with a mean Dice similarity coefficient (DSC) of $89.3 \pm 3.2\%$ for the whole gland (WG), $82.2 \pm 3.0\%$ for the CG, and $69.1 \pm 6.9\%$ for the PZ in 3D body-coil MR images; $89.2 \pm 3.3\%$ for the WG, $83.0 \pm 2.4\%$ for the CG, and $70.0 \pm 6.5\%$ for the PZ in 3D endo-rectal coil MR images. In addition, the experiments of intra- and inter-observer variability introduced by user initialization indicate a good reproducibility of the proposed approach in terms of volume difference (VD) and coefficient-of-variation (CV) of DSC.

© 2014 Elsevier B.V. All rights reserved.

1. Introduction

Prostate cancer is the most common non-skin cancer in men, with one in six men affected during their lifetime (Siegel et al., 2012). Magnetic resonance (MR) imaging is capable of providing a superior visualization of the prostate gland, its substructures and the surrounding tissues (Leslie et al., 2012; Doyle et al., 2012) compared to the traditional transrectal ultrasound (TRUS) imaging in order to better guide and monitor image guided prostate interventions. However, it is costly and time-consuming. The fusion technique of 3D TRUS and MRI for prostate biopsy shares the advantages of both imaging modalities to target biopsy needles effectively in 3D TRUS images toward prostate regions (Qiu et al., 2013e), especially those containing MR identified suspicious lesions. This approach is regarded as an alternative to the more

expensive and inefficient MRI-based prostate biopsy (Beyersdorff et al., 2005).

The prostate consists of four major zones: peripheral zone (PZ), central zone (CZ), transition zone (TZ), and anterior fibromuscular tissue (AFT) (see Fig. 1) (McNeal, 1981). The PZ was obtained by subtracting the central gland (CG) including CZ and TZ from the prostate whole gland (WG) (Villeirs and De Meerleer, 2007). The PZ harbors 70–80% of prostate adenocarcinoma (Pca) (Haffner et al., 2009; Mazaheri et al., 2009) and is a target for prostate biopsy. Typically, there is no clear boundary between CG and PZ in 3D TRUS images (Qiu et al., 2012, 2013d). In contrast, the prostate appears as two visible zones in 3D MR images: the CG and the PZ (see Fig. 2(a)). Superimposing the 3D TRUS guided biopsy image onto the pre-segmented regions of interest in an MR image increases the accuracy of prostate biopsy (Sonn et al., 2013) and therefore sought-after is highly desired in a fused 3D TRUS/MRI guided biopsy system. An essential role of this technique is to accurately and efficiently segment the prostate into the CG and PZ regions. Moreover, the latest change in prostate cancer diagnosis

* Corresponding author.

E-mail address: wqiu@robarts.ca (W. Qiu).

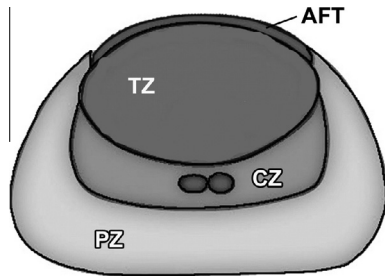


Fig. 1. Prostate anatomy. CG: central gland, TZ: transition zone, CZ: central zone, PZ: peripheral zone, AFT: anterior fibromuscular tissue.

focuses on the detection of small tumors and improvements of cancer staging. In this context, the correct characterization of prostate tissues and structures is a critical step for computer aided diagnosis (CAD) techniques since the occurrence and appearance of cancer is dependent on its zonal location (Niaf et al., 2012). In addition, the ratio of CG volume to whole prostate gland (WG) can be a useful tool for monitoring prostate hyperplasia (Kirby and Gilling, 2011).

1.1. Previous studies

Extensive studies were devoted to segmenting the whole prostate gland from 3D T2-weighted (T2w) MR images (see Ghose et al. (2012) for a literature survey). However, only a few of these focused on prostate zonal segmentation from 3D MR images. Allen et al. (2006) proposed a method to automatically delineate the prostate boundary and CG. However, their method can only segment the middle region of the prostate, and neglects the apex and base of the gland. Yin et al. (2012) proposed an automated CG segmentation algorithm based on layered optimal graph image segmentation of multiple objects and surfaces (LOGISMOS), and reported a mean Dice similarity coefficient (DSC) of 80% for CG from T2W MR images. Both these two studies aimed at only segmenting the CG and ignored the PZ, which limited their application in clinical use. Makni et al. (2011) reported the first study about segmenting both the PZ and CG of the prostate. They used a modified version of the evidential C-means algorithm to cluster voxels into their respective zones by incorporating additional multispectral MR imaging information, which required analyzing the T2w image, the diffusion weighted image (DWI), and the contrast enhanced MR image (CEMRI). The mean DSCs for the PZ and CG of $76.0 \pm 6.0\%$ and $87.0 \pm 4.0\%$ were reported in the study of Makni et al. (2011). More recently, Litjens et al. (2012) proposed a pattern recognition method to classify the voxels using anatomical,

intensity and texture features in multispectral MR images. However, in Makni et al. (2011) and Litjens et al. (2012), prostate zonal segmentation methods require manual segmentation of the whole prostate gland as an initialization, which is arduous and time-consuming. In Litjens et al. (2012), the authors additionally stated that they also developed two atlas-based methods to segment the prostate zones from multispectral MR images at the same time without manually extracting the whole prostate region, which generated mean DSCs of $57.0 \pm 19.0\%$ and $48.0 \pm 22\%$ with respect to the PZ segmentation. The closest work by Toth et al. (2013) used active appearance models with multiple coupled level sets to simultaneously segment prostatic zones, yielding a mean Dice similarity coefficient of 81%, 79% and 68% for WG, CG, and PZ, respectively. They reported the first work exploring a fully automated CG and PZ segmentation algorithm from 3D T2w MR images. However, they validated the algorithm using only 3D T2w MR images with an endo-rectal coil, which have better image quality than 3D T2w MR images with a body-coil. In addition, segmentation results in Toth et al. (2013) relied on the image quality and the number of training images, and their C++ implemented algorithm required more than 3 min to segment a given image.

In this study, a new global optimization-based multi-region segmentation approach is proposed to extract the whole prostate gland and its two sub-regions: the central gland (CG) and peripheral zone (PZ), simultaneously from a single 3D T2w MR image, without incorporating information from multi-spectral MR images.

1.2. Contributions

In this paper, we focus on a global optimization based segmentation approach, the continuous max-flow approach (Yuan et al., 2010a,b), and develop and implement a new algorithm with the integration of a geometrical constraint. Yuan et al. (2010a) provided a continuous max-flow algorithm framework, but have not taken into account geometrical constraints and an object appearance model. Compared to local optimization based methods, such as edge-based active contour (Kass et al., 1988) that is sensitive to initialization and easily trapped in local minima due to false edge information and image noise, and region-based level set (Chan and Vese, 2001) requiring a highly complicated numerical implementation and a small step-size of each iteration to achieve numerical stability of convergence, the proposed approach is capable of moving the contour to its globally optimal position at each discrete time. In contrast to the traditional global optimization methods, such as graph cut, the proposed method avoids metrication artifacts that are present in graph cut-based approaches, and is capable of achieving a better numerical performance in terms of efficiency and memory load.

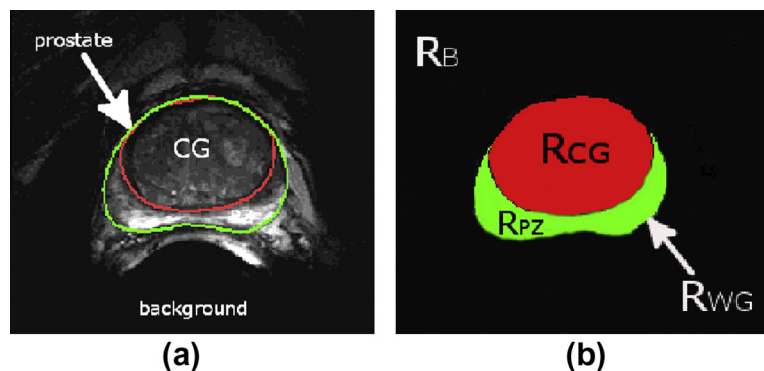


Fig. 2. Contours overlaid on a T2w prostate MRI slice (a) and proposed layout of anatomically consistent regions (b). The prostate region \mathcal{R}_B is divided into two sub-regions: central gland \mathcal{R}_{CG} and peripheral zone \mathcal{R}_{PZ} and is mutually distinct from the background \mathcal{R}_B .

Our main contributions are as follows:

- The proposed method utilizes prior knowledge of the spatial region consistency (WG includes CG and PZ, and CG and PZ are not overlapping, see Fig. 2(b)), and employs a customized prostate appearance model (intensity probability density functions), to segment multiple regions simultaneously.
- A novel spatially continuous flow-maximization formulation is proposed, which is proven to be dual/equivalent to the studied convex relaxed optimization problem with the region consistency constraint. Thus, the original optimization problem can be solved indirectly by maximizing the equivalent continuous flow-maximization formulation with the implicitly encoded specified prostate region layout, which avoids tackling the challenging prostate region layout constraint explicitly.
- The proposed continuous flow-maximization formulation results in a new and efficient *continuous max-flow based* algorithm, which enjoys great advantages in numerics and can be readily implemented on GPUs.

A preliminary study of this work was described in a conference paper (Qiu et al., 2013b), where the algorithm was briefly explained and validated only with a limited number of images. In this paper, we describe both the comprehensive theory of the proposed approach and its detailed implementations. Moreover, in comparison to the preliminary study, the proposed algorithm is validated extensively in terms of accuracy, efficiency, and intra- and inter-observer variability using not only 3D body-coil MR images but also 3D endo-rectal coil MR images.

2. Methods

2.1. Segmentation pipeline

The segmentation pipeline of the proposed 3D prostate segmentation method is shown in Fig. 3. The segmentation of the given 3D MR prostate image is initialized first using 10–12 prostate boundary points, which are positioned on the axial and sagittal views, and fitted to the two closed surfaces corresponding to CG and WG respectively. The details of initialization are addressed in Section 3.2. Based on the two initialized surfaces of CG and WG, the intensity probability density functions (PDFs) associated with three sub-regions (background, CG, PZ) are then approximated from the intensities of voxels partitioned by these two initialized surfaces, which work as the respective appearance models for the following multi-region segmentation process. We particularly impose the anatomical layout of the prostate sub-regions as the essential region-consistency prior to facilitate the joint segmentation of the prostate WG and its sub-regions, i.e., CG and PZ. It results in a challenging combinatorial optimization problem subject to the specified region-consistency prior. In this work, we

propose a novel convex relaxation approach to tackle the studied optimization problem, and introduce an efficient duality-based convex optimization scheme which properly avoids directly tackling the non-smooth energy functional, by simple projections instead, and incorporates the region-consistency constraint implicitly. Moreover, the proposed dual optimization algorithm can be readily implemented on GPUs to achieve a significant speed-up in computation.

2.2. Region consistency constraint

We aim to simultaneously segment a single 3D T2w prostate MR image $I(x)$ into the whole prostate gland, \mathcal{R}_{WG} , and its two mutually distinct sub-regions: the central gland \mathcal{R}_{CG} , and the peripheral zone \mathcal{R}_{PZ} , (see Fig. 2(b)). The anatomical region prior can be essentially represented by

$$\Omega = \mathcal{R}_{WG} \cup \mathcal{R}_B, \quad \mathcal{R}_{WG} \cap \mathcal{R}_B = \emptyset \quad (1)$$

where \mathcal{R}_B denotes the background and the two spatially disjoint sub-regions \mathcal{R}_{CG} and \mathcal{R}_{PZ} constitute the whole gland region \mathcal{R}_{WG} :

$$\mathcal{R}_{WG} = \mathcal{R}_{CG} \cup \mathcal{R}_{PZ}; \quad \mathcal{R}_{CG} \cap \mathcal{R}_{PZ} = \emptyset. \quad (2)$$

2.3. Region appearance models

Given the 3D prostate MR image $I(x)$, let $\pi_i(I(x))$, $i \in \{CG, PZ\}$, be the approximate intensity probability density function (PDF) of the respective prostate sub-region \mathcal{R}_i , and $\pi_B(I(x))$ be the PDF of the background region \mathcal{R}_B (magenta curve in Fig. 5), see Section 3.2 for the details of initialization. Such intensity PDF models provide the global descriptor of the objects of interest in statistics, which can be learned from either the sampled pixels or the given training datasets. Typically, the appearance models, i.e., the intensity PDFs, of the two prostate sub-regions \mathcal{R}_{CG} (green curve in Fig. 5) and \mathcal{R}_{PZ} (red curve in Fig. 5) are distinct from each other, which represent a composite appearance description of the entire prostate region \mathcal{R}_{WG} (blue curve in Fig. 5). This makes it challenging to directly extract the boundaries of \mathcal{R}_{WG} from the given prostate MR image without any further prior appearance knowledge, and, in turn, identify its inherent sub-regions of \mathcal{R}_{CG} and \mathcal{R}_{PZ} correctly. In this regard, we propose to encode the complex appearance model of \mathcal{R}_{WG} by the distinct intensity appearances of \mathcal{R}_{CG} and \mathcal{R}_{PZ} , and integrates *a priori* knowledge (1) and (2) of the anatomical consistency of the prostate-associated regions, as the customized region constraint, to facilitate the segmentation process.

In practice, the separated appearance models of \mathcal{R}_{CG} and \mathcal{R}_{PZ} can be obtained more accurately and easily than the direct mixture appearance PDF model of \mathcal{R}_{WG} for which an accurate sampling statistics is required. Moreover, such a composite intensity appearance model is shown to be more accurate and robust than the often-used mixture appearance model (Delong et al., 2011). Careful designs of the sub-regions, their geometric association and corre-

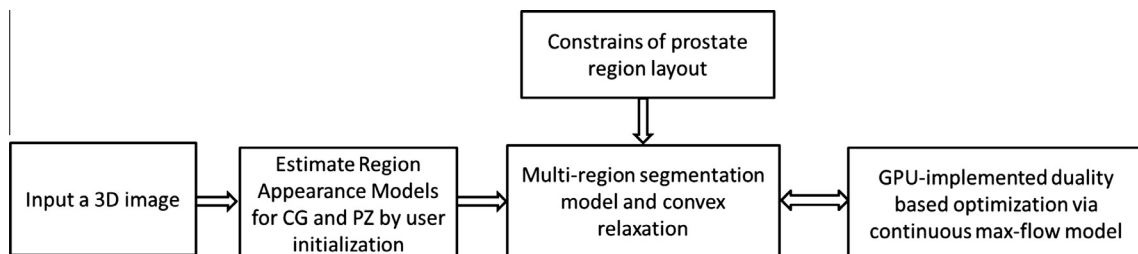


Fig. 3. Segmentation pipeline.

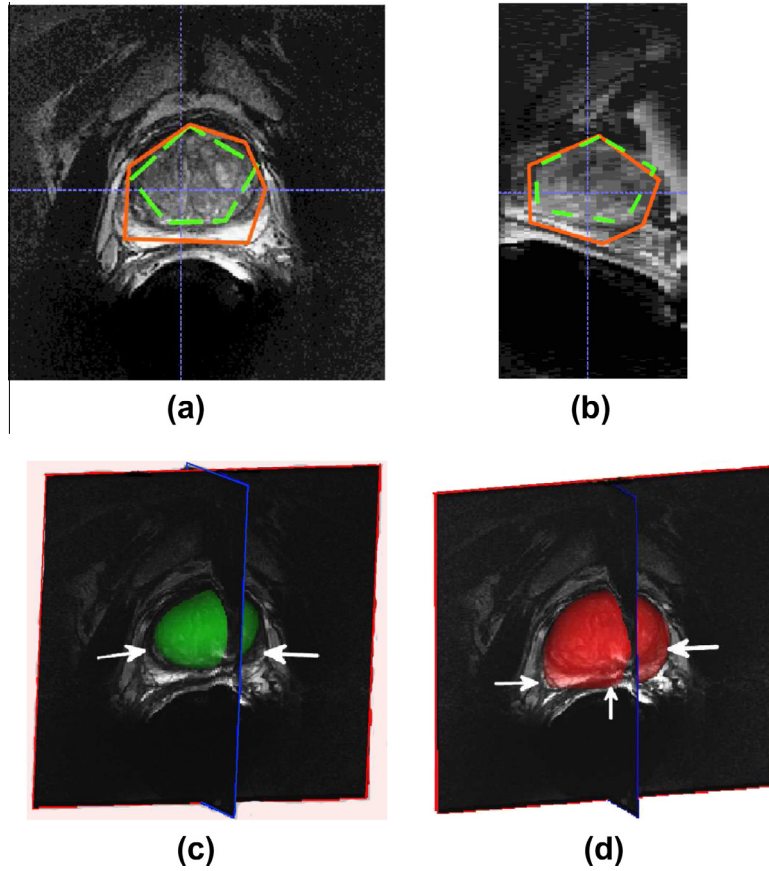


Fig. 4. The scheme for initialization. (a) Axial view, (b) Sagittal view, (c) and (d) orthogonal view overlapped with an initial thin-plate-spline fitted CG and WG surface, respectively. (a) and (b) show polygons generated by user-selected points for WG (red), and CG (green). Arrows show the regions where initial surfaces do not agree well with the actual prostate boundary. (For interpretation of the references to color in this figure legend, the reader is referred to the web version of this article.)

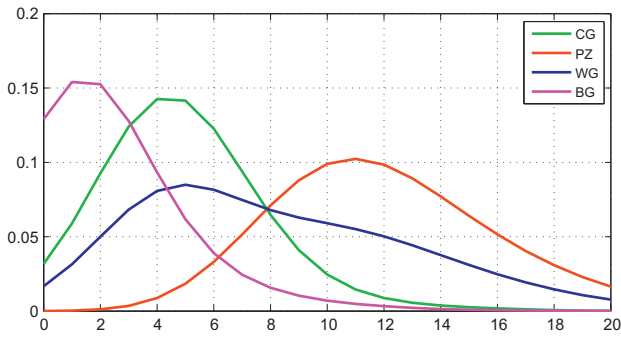


Fig. 5. Typical intensity probability density function (PDF) models of different regions in a 3D prostate T2w MR image. Green: CG, blue: the whole prostate gland, red: PZ, and magenta: background. (For interpretation of the references to color in this figure legend, the reader is referred to the web version of this article.)

sponding appearance models are capable of describing each complex image object in a more robust and accurate way.

Given the intensity PDF $\pi_i(I(x))$, where $i \in L := \{CG, PZ, B\}$, of the region \mathcal{R}_i , we define the cost function $D_i(x)$ of labeling any pixel $x \in \Omega$ to be in the prostate sub-region \mathcal{R}_{CG} , \mathcal{R}_{PZ} or the background region \mathcal{R}_B by the log-likelihood of the respective PDF (Boykov and Jolly, 2001), i.e.,

$$D_i(x) = -\log(\pi_i(I(x))), \quad i \in L := \{CG, PZ, B\}.$$

Consequently, the total labeling cost of segmenting the input prostate MRI $I(x)$ into the following regions

$$\mathcal{R}_{WG} \cup \mathcal{R}_B := \{\mathcal{R}_{CG} \cup \mathcal{R}_{PZ}\} \cup \mathcal{R}_B,$$

can be formulated by

$$\sum_{i \in L} \int_{\mathcal{R}_i} D_i(x) dx. \quad (3)$$

2.4. Multi-region segmentation model and convex relaxation

In this work, we propose to partition the given 3D image $I(x)$ by achieving the minimum total labeling cost (3) along with the minimum total area of all the segmented regions, such that

$$\min_{\mathcal{R}_{WG}, \mathcal{R}_B, \mathcal{R}_{CG}, \mathcal{R}_{PZ}} \sum_{i \in L} \int_{\mathcal{R}_i} D_i(x) dx + \sum_{i \in WG \cup L} \int_{\partial \mathcal{R}_i} ds \quad (4)$$

subject to the constraints of the region layout (1) and (2). Typically, the minimization of total area of the segmented regions is a problem of geodesic computation in a Riemannian space. Solving this minimization problem consists of finding the path of minimal new length, i.e., smooth boundaries. A minimizer will be obtained when the contour is on the boundary of the object. The geodesic active contour model has been widely used in level set based methods (Chan and Vese, 2001).

Let $u_i(x) \in \{0, 1\}$, $i \in \{WG, CG, PZ, B\}$, be the indicator or labeling function of the corresponding region \mathcal{R}_i , such that

$$u_i(x) := \begin{cases} 1, & \text{where } x \text{ is inside } \mathcal{R}_i \\ 0, & \text{otherwise} \end{cases}.$$

Then, we can identically rewrite the region constraint (1) as

$$u_{WG}(x) + u_B(x) = 1, \quad \forall x \in \Omega \quad (5)$$

and the constraint (2) of the prostate sub-regions by

$$u_{CG}(x) + u_{PZ}(x) = u_{WG}(x), \quad \forall x \in \Omega. \quad (6)$$

Correspondingly, the optimization problem (4) can be reformulated in terms of the defined labeling functions $u_i(x) \in \{0, 1\}$, $i \in \{WG, CG, PZ, B\}$, as follows

$$\min_{u(x) \in \{0,1\}} \sum_{i \in L} \langle u_i, D_i \rangle + \sum_{i \in WG \cup L} \int_{\Omega} g_i(x) |\nabla u_i(x)| dx \quad (7)$$

subject to the labeling constraints (5) and (6), where $g_i(x) \geq 0$ gives the non-negative edge weight function and each weighted total-variation function of (7) measures the weighted area of the surface $\partial \mathcal{R}_i$, $i \in WG \cup L$.

Motivated by the recent developments of convex optimization-based image segmentation (Lellmann et al., 2009; Yuan et al., 2010b; Ukwatta et al., 2013; Qiu et al., 2013a,c), we propose to solve the challenging combinatorial optimization problem (7) by its convex relaxation:

$$\min_{u(x) \in [0,1]} \sum_{i \in L} \langle u_i, D_i \rangle + \sum_{i \in WG \cup L} \int_{\Omega} g_i(x) |\nabla u_i(x)| dx \quad (8)$$

subject to the linear equality constraints (5) and (6), where the binary-valued labeling function $u_i(x) \in \{0, 1\}$, $i \in WG \cup L$, in (7) is relaxed into the convex-set constraint $u_i(x) \in [0, 1]$ in (8). Given the convex energy function of (8) and the linear equality constraints (5) and (6), the challenging combinatorial optimization problem (7) is then reduced to its convex optimization version (8) which is much simpler to be optimized.

2.5. Dual optimization model

Inspired by the efficient duality-based optimization schemes proposed in Yuan et al. (2013, 2010b), we introduce a new continuous max-flow approach to solving the proposed convex relaxed multi-region segmentation problem (8) with the constraints (5) and (6), and show the introduced new spatially continuous max-flow formulation is dual to the studied (8).

Similar as the continuous max-flow formulations proposed in Yuan et al. (2010a,b), we first introduce the spatially continuous flow settings as follows (Fig. 6 shows the associated simplified one-voxel graph corresponding to Fig. A.11):

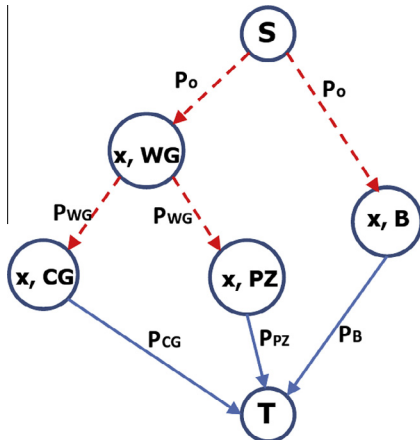


Fig. 6. The flow settings for the proposed continuous flow-maximization scheme (see Fig. A.11 for the one-pixel setting).

- We add two terminals s and t as the source and sink of the flows, the two image copies Ω_{WG} and Ω_B (w.r.t. \mathcal{R}_{WG} and \mathcal{R}_B) and the two image copies Ω_{CG} and Ω_{PZ} (w.r.t. the prostate sub-regions \mathcal{R}_{CG} and \mathcal{R}_{PZ}).
 - We link the source s to the same position x of Ω_{WG} and Ω_B , along which an unconstrained source flow $p_o(x)$ is defined. We link any $x \in \Omega_{WG}$ to the same position x at each of Ω_{CG} and Ω_{PZ} , along which an unconstrained prostate flow $p_t(x)$ is defined. In addition, we link each pixel x of Ω_B and $\Omega_{CG, PZ}$ to the sink t , along which the respective sink flow $p_i(x)$, $i \in L$, is given.
 - Additionally, the spatial flow $q_i(x)$, $i \in WG \cup L$, is specified at any x within the image domain Ω_i .
- Based upon the above settings of flows, the novel *continuous max-flow model*, which maximizes the total flow streaming from the source s to the sink t , can be formulated as follows:

$$\max_{p,q} \int_{\Omega} p_o(x) dx \quad (9)$$

subject to

- *Flow capacity constraints*: the sink flows $p_i(x)$, $i \in L$ suffice:

$$p_i(x) \leq D_i(x), \quad i \in L, \quad (10)$$

and the spatial flows $q_i(x)$, $i \in WG \cup L$ suffice:

$$|q_i(x)| \leq g(x), \quad i \in WG \cup L. \quad (11)$$

- *Flow conservation constraints*: the total flow residue vanishes at each x of the image domain Ω_{WG} or Ω_B , i.e.,

$$G_i(x) := (\text{div } q_i - p_o + p_i)(x) = 0, \quad i \in \{WG, B\}; \quad (12)$$

and the total flow residue also vanishes at each x of the image domain Ω_{CG} or Ω_{PZ} , i.e.,

$$G_i(x) := (\text{div } q_i - p_{WG} + p_i)(x) = 0, \quad i \in \{CG, PZ\}. \quad (13)$$

As defined above, the source flow function $p_o(x)$ and the prostate flow function $p_t(x)$ are both free of constraints. We can prove the duality between the new *continuous max-flow model* (9) and the *convex relaxed optimization problem* (8):

Proposition 1. The continuous max-flow model (9) and the convex relaxed optimization model (8) are dual (equivalent) to each other, i.e.,

$$(9) \iff (8).$$

Proof is given in Appendix B.

Proposition 1 shows that the *convex relaxed optimization problem* (8) can be solved equally by computing the *continuous max-flow formulation* (9). In addition, this derives a new optimization algorithm based on the proposed dual formulation (9), through modern convex optimization techniques (Bertsekas, 1982); hence amounts to the *duality-based optimization algorithm*. The numerical details are given in Appendix C. In practice, the proposed *duality-based optimization algorithm* enjoys great numerical advantages and high computational efficiency (see Appendix C for details).

3. Experiments

3.1. Image acquisition

We evaluated the proposed continuous max-flow algorithm on 18 T2w MR images obtained using a phased-array body coil and 25 T2w MR images obtained using a disposable endo-rectal coil (BPX30, MEDRAD, INC). Subjects were scanned at 3 Tesla with a GE Excite HD MRI system (Milwaukee, WI, USA). Each subject provided written informed consent, which was approved by the Research Ethics Board of The University of Western Ontario. All

images were acquired at $512 \times 512 \times 36$ voxels with a voxel size of $0.27 \times 0.27 \times 2.2$ mm³. Since the endo-rectal coil MR images have better image quality but more motion artifacts compared to body-coil MR images, we validated the proposed approach separately in these two different kinds of images in order to better evaluate the robustness and applicability of our algorithm.

3.2. Initialization

The proposed approach was initialized by two closed surfaces, each of which was constructed via a thin-plate spline fitting with ten to twelve initial points chosen by the user: half on the axial view and half of the points on the sagittal view (see Hu et al. (2003) and Yuan et al. (2012) for more details). Fig. 4 shows an example of initialization for the WG and CG surfaces. The intensity PDFs associated with three sub-regions (background, CG, PZ) are estimated from the intensities of voxels partitioned by the two fitted surfaces, serving as a region appearance model for optimization. In addition, the fitted surfaces also provide auxiliary information of prostate location. More specifically, the original input 3D image was cropped by a bounding box, which was obtained by enlarging the bounding box of the initial WG surface by 30 voxels in each component direction. Based on our experiments, a minimum of ten points are needed to fit such a surface in order to obtain useful results, with five points on the axial view and five points on the sagittal view. More initialization points lead to a more accurate fitted surface, but require more interaction time. Ten to twelve points were typically used in our experiments. In the following experiments, the variability introduced by manual initialization is investigated across different repetitions and different users.

3.3. Evaluation metrics

We evaluated the proposed segmentation method by comparing the algorithm (V_A) to manual segmentation (V_M) results using two region-based metrics: Dice similarity coefficient (DSC) (Zijdenbos et al., 1994):

$$\text{DSC} = \frac{2(V_A \cap V_M)}{V_A + V_M} \times 100\%, \quad (14)$$

which is a measurement of the overlap of the two regions; and sensitivity (Se) (Garnier et al., 2011):

$$\text{Se} = \frac{V_A \cap V_M}{V_M} \times 100\%, \quad (15)$$

which is a measurement of the proportion of true volume, which is correctly identified by the tested method. We denote the manual contour M as a set of vertices $\{m_i : i = 1, \dots, K\}$, the algorithm-generated contour A as the set of vertices $\{a_i : i = 1, \dots, N\}$, and $d(m_i, A)$ as the distance between vertex m_i of contour M and its closest vertex on contour A . The mean absolute surface distance (MAD)

$$\text{MAD} = \frac{1}{K} \sum_{i=1}^K d(m_i, A), \quad (16)$$

and the Hausdorff distance (MAXD)

$$\text{MAXD} = \max_{i \in [1, K]} \{d(m_i, A)\}, \quad (17)$$

were used as distance-based metrics (Ukwatta et al., 2013; Qiu et al., 2012). Volume difference (VD) (Ding et al., 2007): $\text{VD} = |V_A - V_M|$, was also used to evaluate the absolute volume difference between manual and algorithm segmented volumes, which is clinically important for volume estimation, dose escalation and implant quality assessment for brachytherapy (Smith et al., 2007). Each prostate image was divided into three sub-regions, base,

mid-gland and apex, according to the apex-base axis of the manual segmented prostate surface (respectively, 0.3, 0.4, 0.3 length fraction of the base-apex axis) (Mahdavi et al., 2011). All validation metrics were calculated for the prostate gland, central gland and peripheral zone in the three respective regions. In addition, the coefficient-of-variation (CV) (Zou and Mcdermott, 1999) of DSC and VD were used to evaluate the intra- and inter-observer variability introduced by user manual initialization.

It should be noted that all manual segmentations were outlined by a technician and approved by a radiologist with more than ten years of experience. The technician providing manual segmentations was excluded in the intra- and inter-observer variability experiments. To avoid users from remembering a previous segmentation, five days separated re-segmenting the same case in the intra-observer variability test. Two trained graduate students and one trained post-doctoral fellow were involved in the inter-observer variability test.

4. Results

4.1. Accuracy

Figure 7 shows two examples of prostate segmentation from 3D MR images. Table 1 shows the segmentation results for 18 patient images acquired with a body coil using the proposed method. The mean DSC was $89.3 \pm 3.2\%$ for the WG, $82.2 \pm 3.0\%$ for the CG, and $69.1 \pm 6.9\%$ for the PZ. The mean Se for the WG, CG and PZ was slightly higher than the DSC. This table shows that our method is capable of generating good agreement with the manual delineations in the base-, mid- and apex-regions of CG and WG. More specifically, the proposed algorithm yielded the highest DSC of $94.3 \pm 1.5\%$ for the CG mid-region of the prostate. The lowest DSC of $54.5 \pm 20.9\%$ was generated at the PZ base-region of the prostate. However, a DSC of $81.8 \pm 5.0\%$ and a Se of $85.5 \pm 3.5\%$ for mid-PZ are favorable, which could meet clinical requirements. Volume measurements shows that our proposed method generated a mean VD of 2.8 ± 1.6 cm³ for the WG, 2.2 ± 1.5 cm³ for the CG and 2.0 ± 1.7 cm³ for the PZ, compared to the average volume size of 55.4 cm³ for the WG, 42.2 cm³ for the CG, and 13.2 cm³ for the PZ. In addition, Table 1 also shows the evaluation results of the MAD and MAXD, which demonstrate similar consistent information to the DSC and Se.

The evaluation results using the proposed approach for 25 patient images acquired with an endo-coil are shown in Table 2. It shows that the mean DSCs are $89.2 \pm 3.3\%$ for the WG, $83.0 \pm 2.4\%$ for the CG, and $70.0 \pm 6.5\%$ for the PZ, which are slightly greater than the results for MR images with a body-coil. Furthermore, the proposed method is capable of yielding better accuracy in terms of DSC, Se, VD, MAD and MAXD at the base-, mid- and apex-regions of CG, PZ and WG for endo-coil images than for body-coil images.

4.2. Variability

Since the proposed approach requires the user to choose some boundary points for initialization, segmentation variability will result. To investigate the impact of manual initialization, ten randomly selected 3D body-coil and ten 3D endo-coil MR images were used to evaluate the reproducibility of our method. The entire PZ, CG, and WG for each prostate were taken into account instead of their separate sections (i.e., apex, mid and base). Each image was initialized and segmented five times by the same observer to assess intra-observer variability in terms of VD and CV of DSC, and each image was also segmented by two other users to evaluate inter-observer variability (see Fig. 8 and 9).

Table 1
Overall segmentation accuracy for 18 patient 3D MR images with a body-coil, represented as the mean value \pm standard deviation. Results of MAD and MAXD are shown as voxels and corresponding millimeters in brackets.

	Total	Base	Mid	Apex
<i>DSC (%)</i>				
PZ	69.1 \pm 6.9	54.5 \pm 20.9	81.5 \pm 5.2	60.5 \pm 12.3
CG	82.2 \pm 3.0	81.1 \pm 2.9	94.3 \pm 1.5	68.0 \pm 8.1
WG	89.3 \pm 3.2	84.6 \pm 3.4	92.1 \pm 2.6	87.4 \pm 4.8
<i>Se (%)</i>				
PZ	73.2 \pm 6.3	63.2 \pm 16.5	85.5 \pm 3.5	65.2 \pm 8.3
CG	85.5 \pm 2.5	85.2 \pm 2.5	94.8 \pm 1.7	81.1 \pm 5.2
WG	90.0 \pm 3.2	86.5 \pm 3.0	94.5 \pm 2.4	88.6 \pm 3.6
<i>VD (cm³)</i>				
PZ	2.0 \pm 1.7	0.8 \pm 0.7	1.5 \pm 1.3	0.9 \pm 0.8
CG	2.2 \pm 1.5	1.2 \pm 0.8	1.2 \pm 1.1	1.5 \pm 1.0
WG	2.8 \pm 1.6	1.1 \pm 1.2	1.4 \pm 1.3	1.2 \pm 1.1
<i>MAD (voxels (mm))</i>				
PZ	2.6 \pm 0.9 (3.9 \pm 1.2)	4.5 \pm 3.1 (4.9 \pm 1.9)	2.0 \pm 0.7 (2.3 \pm 0.8)	2.1 \pm 1.8 (2.9 \pm 1.1)
CG	2.8 \pm 1.1 (4.1 \pm 1.1)	3.4 \pm 1.4 (4.2 \pm 1.2)	2.1 \pm 0.8 (3.0 \pm 1.0)	3.6 \pm 1.5 (4.7 \pm 1.3)
WG	1.6 \pm 0.7 (3.3 \pm 0.8)	2.5 \pm 1.7 (3.4 \pm 1.2)	3.0 \pm 2.1 (3.3 \pm 1.2)	2.0 \pm 0.8 (2.3 \pm 0.8)
<i>MAXD (voxels (mm))</i>				
PZ	20.5 \pm 14.2 (24.0 \pm 13.2)	35.4 \pm 24.5 (13.8 \pm 7.0)	14.8 \pm 12.7 (13.9 \pm 4.0)	15.5 \pm 9.7 (9.6 \pm 2.6)
CG	15.2 \pm 15.0 (17.2 \pm 6.0)	17.2 \pm 15.5 (11.5 \pm 3.4)	10.6 \pm 4.3 (13.8 \pm 3.7)	20.1 \pm 9.8 (13.4 \pm 3.7)
WG	7.8 \pm 3.8 (13.4 \pm 3.7)	13.5 \pm 10.2 (10.0 \pm 3.0)	15.0 \pm 15.2 (13.0 \pm 3.7)	18.0 \pm 7.0 (10.6 \pm 2.7)

Table 2
Overall segmentation accuracy for 25 patient 3D MR images with an endo-coil, represented as the mean value \pm standard deviation. Results of MAD and MAXD are shown as voxels and corresponding millimeters in brackets.

	Total	Base	Mid	Apex
<i>DSC (%)</i>				
PZ	70.0 \pm 6.5	56.0 \pm 18.2	83.1 \pm 4.7	61.5 \pm 10.5
CG	83.0 \pm 2.4	82.2 \pm 2.6	94.2 \pm 1.6	69.3 \pm 8.2
WG	89.2 \pm 3.3	85.6 \pm 3.1	92.5 \pm 2.3	87.2 \pm 4.6
<i>Se (%)</i>				
PZ	74.5 \pm 6.4	63.5 \pm 15.2	85.4 \pm 3.5	63.6 \pm 8.4
CG	85.6 \pm 2.3	85.2 \pm 2.5	93.5 \pm 1.7	82.3 \pm 4.3
WG	91.3 \pm 3.2	86.5 \pm 3.2	93.4 \pm 2.3	89.0 \pm 3.6
<i>VD (cm³)</i>				
PZ	1.7 \pm 1.8	0.6 \pm 0.7	1.3 \pm 1.2	0.8 \pm 0.8
CG	2.1 \pm 1.5	1.5 \pm 1.4	1.1 \pm 0.8	1.6 \pm 1.0
WG	2.3 \pm 1.5	1.0 \pm 0.8	1.3 \pm 1.2	1.1 \pm 0.7
<i>MAD (voxels (mm))</i>				
PZ	2.3 \pm 0.6 (3.7 \pm 1.2)	4.5 \pm 3.5 (4.8 \pm 2.0)	1.8 \pm 0.8 (2.3 \pm 0.6)	2.4 \pm 1.5 (3.2 \pm 1.4)
CG	2.7 \pm 0.8 (3.9 \pm 1.0)	3.2 \pm 2.1 (4.2 \pm 1.3)	2.0 \pm 1.2 (2.9 \pm 1.1)	3.8 \pm 1.5 (4.8 \pm 1.6)
WG	1.5 \pm 0.6 (3.2 \pm 1.0)	2.3 \pm 1.8 (3.2 \pm 1.3)	3.0 \pm 2.7 (3.1 \pm 1.6)	1.7 \pm 0.7 (2.1 \pm 0.7)
<i>MAXD (voxels (mm))</i>				
PZ	18.5 \pm 13.8 (22.4 \pm 12.6)	34.0 \pm 23.3 (12.0 \pm 8.2)	14.6 \pm 14.5 (12.8 \pm 4.5)	15.0 \pm 10.5 (10.5 \pm 2.6)
CG	14.5 \pm 15.5 (15.5 \pm 6.2)	16.5 \pm 15.5 (12.8 \pm 3.6)	9.6 \pm 4.8 (12.8 \pm 3.6)	18.8 \pm 9.8 (12.8 \pm 3.4)
WG	7.7 \pm 3.8 (11.6 \pm 3.6)	13.4 \pm 11.0 (10.8 \pm 3.3)	14.6 \pm 14.0 (11.6 \pm 3.3)	16.8 \pm 6.5 (9.8 \pm 2.9)

Fig. 8 shows the repeat segmentation results in terms of VD. Five repeat segmentations initialized by the same observer in Fig. 8(a) show the similar VDs for PZ, CG, and WG in 10 3D body-coil MR images. Three single factor one-way ANOVA tests ($\alpha = 0.05$) failed to demonstrate a statistically significant difference in terms of VD among 5 repeat segmentations for PZ

($p < 0.005$), CG ($p < 0.001$), and WG ($p < 0.001$). Three segmentations initialized by three different observers are plotted in Fig. 8(b), which indicates that our proposed algorithm is capable of generating similar results of VD from different observers in 3D body-coil MR images. A single factor one-way ANOVA test ($\alpha = 0.05$) shows that there is no statistically significant difference in terms of VD

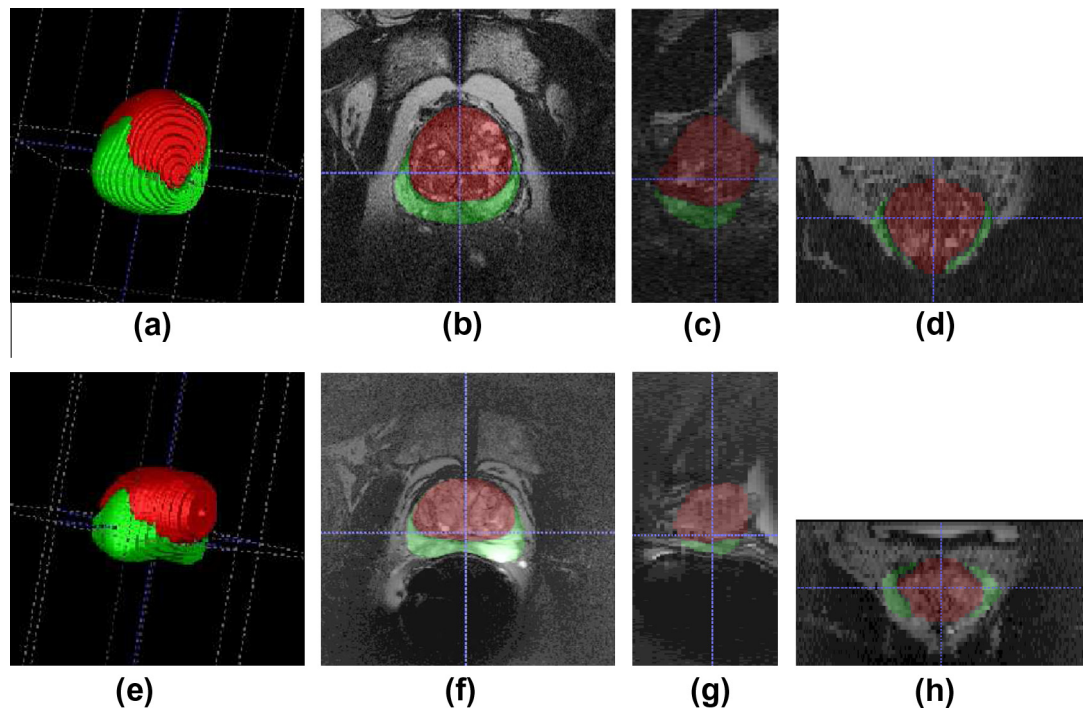


Fig. 7. Segmentation result of two prostates. First row: one prostate segmentation result in a 3D MR image with a body-coil; second row: one prostate segmentation result in a 3D MR image with an endo-coil. Column 1 to column 4: resulting surface, axial view, sagittal view, and coronal view, respectively. Red: the segmented CG, green: the segmented PZ. (For interpretation of the references to color in this figure legend, the reader is referred to the web version of this article.)

among these three segmentations for PZ ($p < 0.005$), CG ($p < 0.001$), and WG ($p < 0.001$). The similar repeat segmentation experiments in terms of VD for endo-coil images in Fig. 8(c) and (d) demonstrate similar results with the experiments for body-coil images.

Fig. 9(a) shows the results for the intra-observer variability for body-coil images in terms of CV of DSC. A mean CV of DSC of 9.3%, 1.7%, and 3.4% were found for PZ, CG, and WG for body-coil images, respectively. The proposed method initialized by three users yielded a mean CV of DSC of 9.63%, 1.8%, and 3.6% for PZ, CG, and WG, respectively (Fig. 9(b)). The results of intra-observer variability for endo-coil images in terms of CV of DSC in Fig. 9(c) show that the proposed approach yielded a mean CV of DSC of 7.3%, 1.1%, and 2.2% for PZ, CG, and WG, respectively, from five repeated segmentations obtained from the same observer. A mean CV of DSC of 7.4%, 0.9%, and 2.3% for PZ, CG, and WG, were obtained from the three observers (Fig. 9(d)).

Both the intra- and inter-observer measurements of the CG and WG for the used datasets in endo- and body-coil images show that the DSC and VD values are consistent and show small variations across different repetitions and different users, but the segmentation variability is higher for PZ. In addition, the proposed method has better reproducibility using the endo-coil than the body-coil images.

4.3. Efficiency

The proposed algorithm was implemented using parallel computing architecture (CUDA, NVIDIA Corp., Santa Clara, CA) and the user interface in Matlab (Natick, MA). The GPU based algorithm was developed with non-optimized Matlab code based on single-thread programming, which was run in serial on a Windows desktop with an 4-core Intel i7-2600 CPU (3.4 GHz) and a NVIDIA GeForce 5800X GPU. The segmentation time was calculated as the mean run time of five repeated segmentations for each 3D MR

image. The mean segmentation time of our method for each patient image was 50 ± 3.5 s in addition to 35 ± 5 s for initialization, resulting in a total segmentation time of less than 1.5 min for each 3D image. It should be noted that the mean segmentation time of 50 ± 3.5 s includes ≈ 30 s for data cost computation that was run on a CPU, and ≈ 20 s for the continuous max-flow computation that was run on a GPU. Note that, this non-optimized Matlab GPU code can be better optimized by vectorizing loops, pre-allocating arrays, and using built-in Matlab functions instead of scripts, etc. We also developed a CPU version for the continuous max-flow computation, which took ≈ 140 s, leading to a total segmentation time of ≈ 205 s with non-optimized CPU-implemented Matlab code.

5. Discussions and conclusions

In this study, we describe and evaluate a novel global optimization based multi-region segmentation approach to extract prostate zones from 3D T2w MR images in a numerically stable and efficient way. The experimental results for both 3D body- and endo-coil MR images show that the proposed algorithm is capable of providing accurate, robust and efficient segmentations in terms of high accuracy and efficiency while achieving low intra- and inter-observer variability introduced by user initializations, for different prostate zones, such as the PZ, CG and WG.

5.1. Comparison with other prostate zonal segmentation methods

Compared to state-of-the-art prostate zonal segmentation methods related to this study, such as the active appearance model based method modified by Toth et al. (2013), C-means algorithm proposed by Makni et al. (2011) and pattern recognition based method reported by Litjens et al. (2012), our methods yield mean DSCs for PZ and CG of $69.1 \pm 6.9\%$ and $82.2 \pm 3.0\%$ in body-coil images, and $70.2 \pm 6.3\%$ and $83.5 \pm 2.5\%$ in endo-coil images,

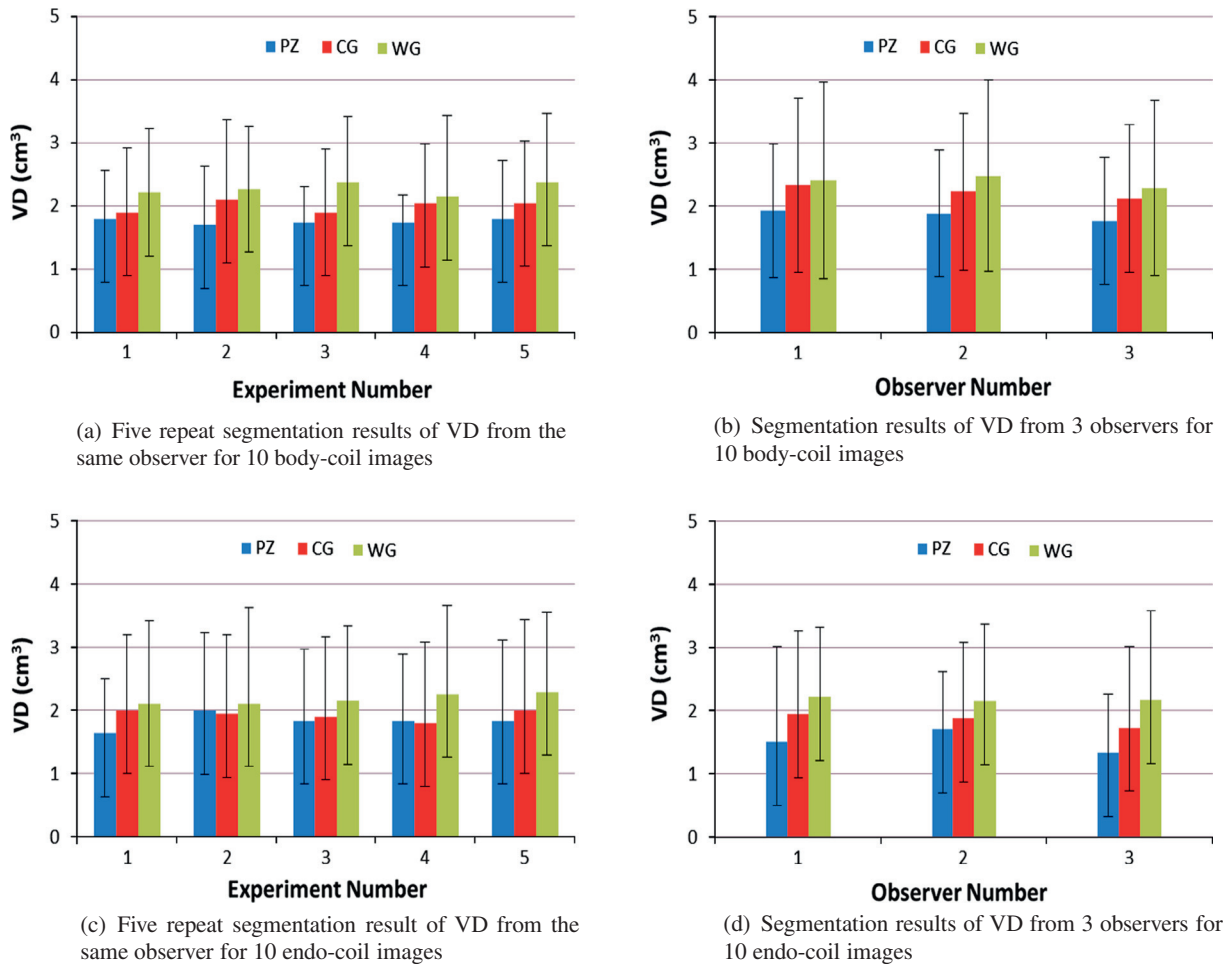


Fig. 8. Results of repeat segmentations in terms of VD to assess the intra- and inter-observer variability for 3D MR body-coil and endo-coil images. The column bars show the mean value, and error bars indicate the standard deviation.

respectively, which are higher than the 68% and 79% reported by Toth et al. (2013), but lower than $75.0 \pm 7.0\%$ and $89.0 \pm 3.0\%$ reported in Litjens et al. (2012) or $76.0 \pm 6.0\%$ and $87.0 \pm 4.0\%$ reported in Makni et al. (2011). However, the methods of Litjens et al. (2012) and Makni et al. (2011) required inputs of 3D multi-spectral MR images, which included a T2w image, a diffusion weighted image and a contrast enhanced MR image. In addition, initialization in both methods required arduous and time-consuming manual segmentation of the. In contrast, our proposed method makes use of only a single 3D T2W MR image as the input and requires much less user interactions for initialization. The automated CG segmentation algorithm based on LOGISMOS proposed by Yin et al. (2012) generated a mean DSC of 80% for CG from T2W MR images without the PZ segmentation, which is lower than the DSC result in our study. Litjens et al. (2012) also mentioned two atlas based zonal segmentation methods without manual segmentation as initialization that generated the mean DSCs of $57.0 \pm 19.0\%$ and $48.0 \pm 22\%$ with respect to PZ segmentation, which are lower than the reported DSC of PZ segmentation by the proposed approach. In addition, we conducted similar experiments using the manual segmentation of the WG for initialization, and validated our proposed method with these initializations using 10 images from the variability testing dataset. The results show a mean DSC of $75.5 \pm 6.2\%$ and $89.2 \pm 3.2\%$ for PZ and CG that are better than the results obtained with the 12-point initialization and comparable to results in Litjens et al. (2012) and Makni et al. (2011).

Although the method proposed by Toth et al. (2013) was implemented in C++, in terms of the computational time it required approximately 200 s to segment one 3D prostate MR image, compared to 80 s by our GPU implementation and 205 s by our CPU implementation. Litjens et al. (2012) and Makni et al. (2011) have not reported their computational time. Implementing the proposed algorithm in C++ and parallelizing the computation of cost function will potentially speed up the segmentation. In this regard, the proposed method demonstrates an advantage for PZ segmentation in terms of accuracy and efficiency. In addition, the low inter- and intra-observer variability in VD and CV of the DSC of the proposed method suggests high reproducibility and independence on the observer, which is particularly useful for multi-center clinical trials.

5.2. Comparison with other prostate whole gland segmentation methods

We compared the proposed method with several approaches to the segmentation of the prostate whole gland (WG) from 3D T2w MR images. Using the data set of MICCAI'2012 Prostate Segmentation Challenge (MICCAI, 2012), the highest mean DSC of $88.0 \pm 3.0\%$ was reported for the prostate WG segmentation (Vincent et al., 2012) which applied active appearance models as the image features for segmentation; but took 8 min per image and 2 additional hours of training. In contrast, the proposed approach performed with slightly better accuracy and demonstrated an

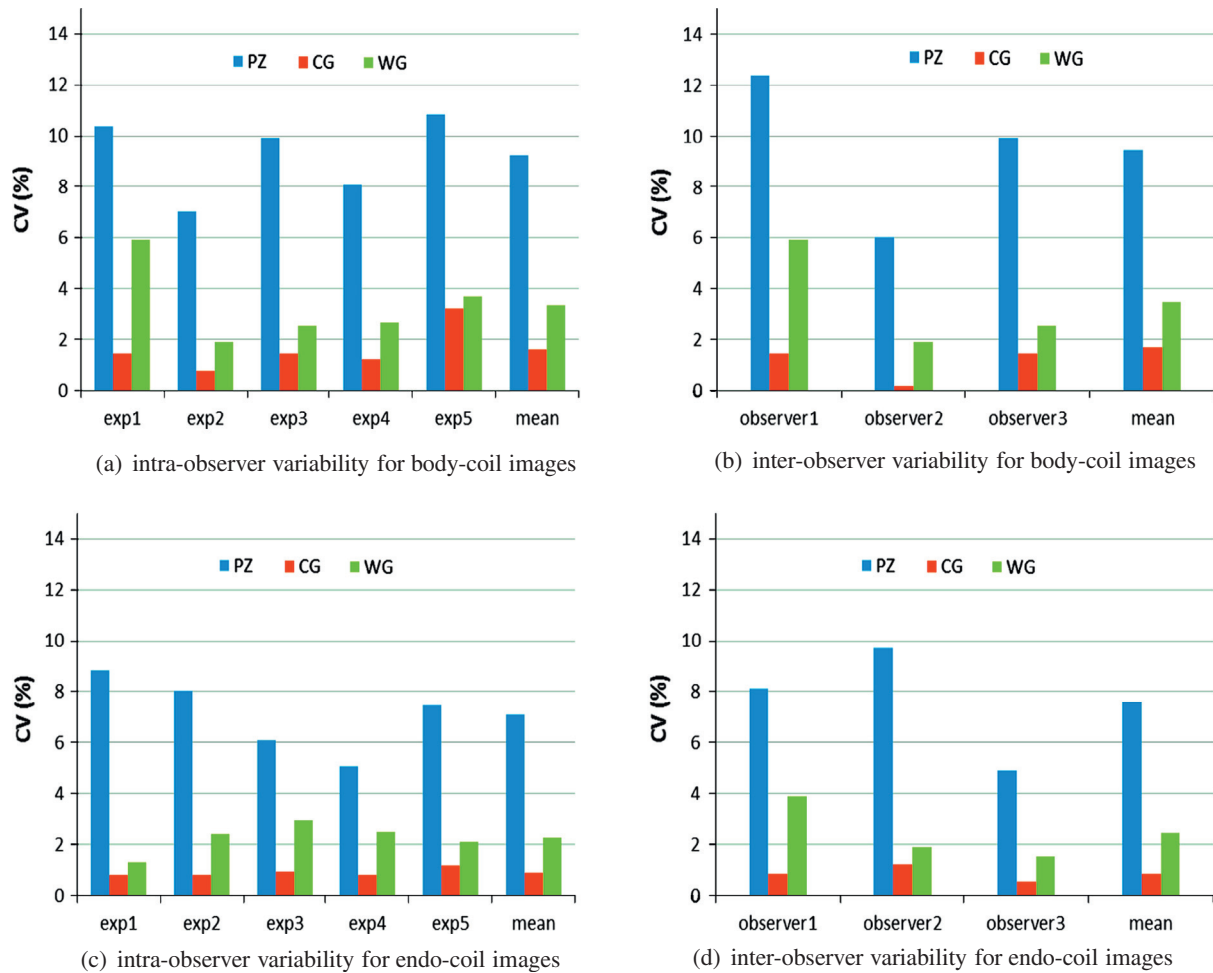


Fig. 9. Result of intra- and inter-observer variability in terms of the coefficient-of-variation (CV) of DSC for 3D MR body-coil and endo-coil images.

advantage in computational efficiency of about 1.5 min for each image). Additionally, Gao et al. (2010) reported a mean DSC of $84.0 \pm 3.0\%$ for their dataset but did not report the segmentation time for their method of combined segmentation with registration. A mean DSC of 86.0% was reported for 36 cases in (Martin et al., 2010). Klein et al. (2007, 2008) reported a median DSC of around 85% on 50 patient images, but it took 15 min per registration, leading to more than one hour to achieve the segmentation result for each image. The Label fusion based prostate segmentation method introduced by Langerak et al. (2010) required more than 8 min to achieve an average DSC of 87%. Although Khalvati et al. (2013) reported a high DSC of 92% for 3D MR prostate images, the computational time required for the segmentation of one prostate image was about 3 min with nonrigid registration. Compared to Martin et al. (2010), Gao et al. (2010), Klein et al. (2008), Langerak et al. (2010), Khalvati et al. (2013), the proposed approach is favorable due to its prostate zonal segmentation and high computational efficiency and a mean DSC of $89.3 \pm 3.2\%$ for bodycoil images and $89.5 \pm 3.2\%$ for endocoil images.

5.3. Comparison with manual segmentation

Compared to manual segmentations, our method's DSCs for the base- and apex-PZ are comparably low and have large standard deviation ($54.7 \pm 20.8\%$ and $60.1 \pm 12.2\%$, respectively) due to the low degree of recognition of such a thin structure

and complicated by partial volume effects and unclear boundaries between zones. Although segmentation for these two regions is highly challenging even for radiologists, manual post-segmentation surface editing for these regions is still required for the proposed method, introducing approximately 1 min of additional time. However, a DSC of $81.8 \pm 5.0\%$ for mid-PZ is favorable, which could meet clinical requirements considering values of DSC above 70% are usually regarded as a satisfactory level of agreement between two segmentations (Zijdenbos et al., 1994; Xue et al., 2007). Additionally, the volume measurement results show that our proposed method generated small values for the mean VD for PZ of 2.0 cm^3 in body-coil images, and 1.7 cm^3 for endo-coil images. The low inter- and intra-observer variability for PZ also indicates a high reproducibility, independent of observers, which is particularly useful for multi-center clinical trials. Moreover, the proposed approach can provide good segmentation accuracy for all prostate sections of both CG and WG, which is highly desirable during image-guided prostate interventions and cancer diagnosis.

Note that the PZ surface was obtained by subtracting the CG surface from the WG surface. The WG and CG surfaces were manually outlined slice-by-slice, which required 8–10 min for each image. In this regard, the computational time of 1.5 min in addition to approximately 1 min of editing required by the proposed approach, is preferable for three-region segmentation. Another significant advantage of the proposed semi-automatic segmentation is that

it requires much less expertise and workload for radiologists compared to manual segmentation.

5.4. Limitations and future work

To further improve the segmentation accuracy in basal and apical regions, future studies will focus on incorporating additional prior information, such as texture and shape or rely on information from multi-spectral MR imaging. In addition, the proposed approach is a semi-automatic algorithm, which requires a few user-selected boundary points for initialization, introducing observer variability. Developing a fully automatic approach remains an important topic, which might be accomplished by improving the initialization step. Possible solutions to a fully-automated segmentation algorithm can be realized with the use of atlas-based methods and machine learning techniques to estimate the approximate location of the prostate and samples for the PDFs. This has been successfully applied in other applications (Wang et al., 2013; Li et al., 2012). Developing such an accurate, efficient and robust fully-automated algorithm is one of our future goals. Another limitation of this study is that volume measurement was performed based only on one image for the single time point for each patient, acquired only from the transverse view. The low resolution of these images in coronal and sagittal views could affect the accuracy of volume measurements. The reproducibility of volume measurements in multiple images acquired from different views for each patient will increase clinical values of this study, which will be investigated in the future. In addition, bias field correction might be used as a pre-processing procedure to improve the segmentation accuracy using the endo-rectal coil MR images. This issue will be addressed in one of our future investigations.

In conclusion, the proposed method provides a fast, accurate and reproducible solution to prostate zonal segmentation from a single 3D T2w MR image. Its reliable performance, combined with minimal user interactions, demonstrates its potential clinical use in 3D TRUS/MR image guided prostate interventions and computer aided diagnosis of prostate cancer.

Acknowledgments

The authors thank Dr. Cesare Romagnoli for helping with the manual prostate segmentation, and Lori Gardi and David Tessier for providing images. The authors are grateful for funding support from the Canadian Institutes of Health Research (CIHR), the Ontario Institute of Cancer Research (OICR), and the Canada Research Chairs (CRC) Program.

Appendix A. Preliminaries on continuous min-cut/max-flow methods

By a series of seminal studies, e.g. (Boykov et al., 2001; Chan et al., 2006), etc., functional minimization has been well established as the paradigm to solve the problems of image segmentation and achieved a great success in practice. For the single region segmentation, i.e., extracting the foreground object from the background, it results in computing the optimum of the following minimization problem:

$$\min_S \int_S D_1(x) dx + \int_{\Omega \setminus S} D_2(x) dx + \int_{\partial S} g(s) ds, \quad (\text{A.1})$$

where S denotes the segmentation region in the given 2D or 3D image domain Ω , $D_{1,2}(x)$ present the two cost functions to label any $x \in \Omega$ as foreground and background respectively, and the last term of (A.1) measures the weighted perimeter (for 2D) and area (for 3D) of the region S . Clearly, the solution to such an optimization

problem (A.1) gives the minimum total cost to label/segment the whole image domain Ω , jointly with the minimum weighted perimeter (in 2D) and area (in 3D).

It was proved that the studied optimization problem (A.1) can be solved globally and exactly, see Chan et al. (2006) and Yuan et al. (2013) for details. In this regard, two essential categories of algorithms were proposed to compute the global optimum of (A.1) in practice:

A.1. Classical min-cut/max-flow methods

One category of algorithms is built upon the spatially discrete setting in terms of min-cut/max-flow over the graph (Boykov et al., 2001; Kolmogorov and Zabih, 2004): Given the graph $G = (V; E)$ consisting of a vertex set V and an edge set $E \subset V \times V$, its vertex set V includes all the nodes on the 2D or 3D image grid and two terminal vertices: the source s and the sink t (see Fig. A.10); its edge set E includes two types of edges: the spatial edges e_n of the given grid, which link two neighboring grid nodes except s and t , and the terminal edges: e_s and e_t , which links the specified terminals s and t to each grid node respectively; a cost $C(e)$ is assigned to each edge e ; a cut divides the spatial grid nodes into two disjoint sets: one relates to the source s and the other to the sink t , the energy of such cut is the total cost of edges e , for which end-points belong to two different partitions; a *min-cut* is to find the two partitions of vertices such that the corresponding cut-energy is minimal.

It was proved by the classical graph optimization theory that resolving the min-cut over a graph is mathematically equivalent to computing its associated max-flow. In fact, most efficient min-cut algorithms were developed based upon such a flow-maximization scheme, i.e., determining the maximum flow over the graphs: Each edge e can be viewed as a pipe and the edge cost $C(e)$ can be regarded as the capacity of this pipe; the max-flow over the graph tries to find the largest flow streaming from the source s : once the maximum flow is achieved, the min-cut can be determined by all the edges with saturated/maximum-allowed flow.

A.2. Continuous min-cut/max-flow methods

The second category of algorithms is built in the spatially continuous setting, along with continuous variational analysis, the optimization problem (A.1) can be directly formulated as the following combinatorial optimization problem, i.e., also called the *continuous min-cut problem*:

$$\min_{u(x) \in \{0,1\}} \int_{\Omega} (uD_1 + (1-u)D_2) dx + \int_{\Omega} g(x) |\nabla u| dx \quad (\text{A.2})$$

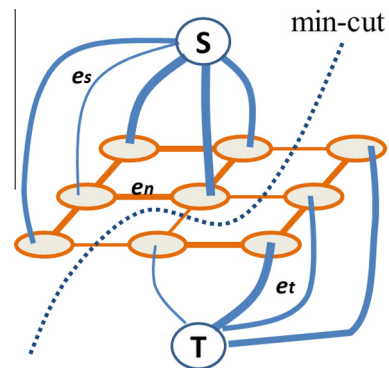


Fig. A.10. The classical min-cut/max-flow scheme over graphs.

where the binary function $u(x) \in \{0, 1\}$ denotes the indicator/labeling function of the region S in (A.1), accordingly, the weighted perimeter/area term in (A.1) is expressed by the weighted total-variation term in (A.2); by the recently developed convex relaxation theory, it was shown (Chan et al., 2006; Yuan et al., 2010a) that the challenging continuous min-cut problem (A.2) can be solved globally and exactly by its convex relaxation:

$$\min_{u(x) \in [0,1]} \int_{\Omega} (uD_1 + (1-u)D_2)dx + \int_{\Omega} g(x)|\nabla u|dx \quad (\text{A.3})$$

where the binary labeling constraint $u(x) \in \{0, 1\}$ in (A.2) is relaxed to the convex constraint of $u(x) \in [0, 1]$, such that (proposed firstly in Chan et al. (2006), then Yuan et al. (2010a)):

Proposition 2. Let $u^*(x)$ be the global optimum of the convex relaxation problem (A.3). Then given each α -upper level set $S^\alpha := \{x | u^*(x) \geq \alpha\}$, for $\forall \alpha \in (0, 1]$, of $u^*(x)$, its indicator function $u^\alpha(x)$

$$u^\alpha(x) := \begin{cases} 1, & u^*(x) \geq \alpha \\ 0, & u^*(x) < \alpha \end{cases},$$

is a global binary solution of the continuous min-cut problem (A.2).

As demonstrated in Proposition 2, it is very interesting that thresholding the computed optimum of the convex relaxed continuous min-cut problem (A.3) by the parameter $\alpha \in (0, 1]$ generates the globally optimal segmentation result to the continuous min-cut problem (A.2). Hence, the difficult combinatorial optimization problem (A.2) can be solved by computing its convex relaxation (A.3) which is much simpler in numerics.

Motivated by such duality between the classical min-cut and max-flow problems, Yuan et al. (2010a, 2013) introduced a novel continuous max-flow formulation to the convex relaxed continuous min-cut problem (A.3), and showed the duality between the proposed continuous max-flow model and (A.3) using modern variational analysis.

In Yuan et al. (2010a, 2013), a flow maximization configuration in the spatially continuous setting is first introduced (as shown in Fig. A.11: the left-side picture shows the detailed flow settings whereas the right-side shows the simplified graph over one pixel), which is similar as the classical max-flow (see Fig. A.10):

- Given the image Ω , two terminals s and t as the source and sink of the flows are added; link the source s to any pixel x of Ω , along which the source flow $p_s(x)$ is defined from s to x ; link any pixel $x \in \Omega$ to the sink t , along which the sink flow $p_t(x)$ is defined from x to t .
- Additionally, the spatial flow $q(x)$ is specified at any pixel $x \in \Omega$. Based upon the above flow settings, the *continuous max-flow formulation* is proposed, which maximizes the total flow streaming from the source s to the sink t , i.e.,

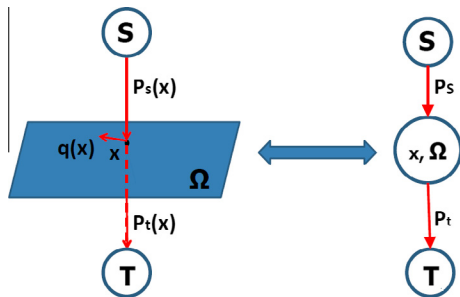


Fig. A.11. The leftside graph shows the spatially continuous max-flow settings, which is similar as the configuration of the classical max-flow demonstrated in Fig. A.10; the rightside graph shows the simplified version of the continuous max-flow settings over the one-pixel setting.

$$\max_{p,q} \int_{\Omega} p_s(x)dx \quad (\text{A.4})$$

subject to

– *Flow capacity constraints:* the source flow $p_s(x)$ and the sink flow $p_t(x)$ suffice:

$$p_s(x) \leq D_2(x), \quad p_t(x) \leq D_1(x), \quad (\text{A.5})$$

and the spatial flow $q(x)$ suffices:

$$|q(x)| \leq g(x). \quad (\text{A.6})$$

– *Flow conservation constraints:* the total flow residue vanishes at each pixel $x \in \Omega$, i.e.,

$$(\text{div } q - p_s + p_t)(x) = 0. \quad (\text{A.7})$$

In mathematics, Yuan et al. (2010a, 2013) demonstrated that the proposed continuous max-flow model (A.4) is dual/equivalent to the convex relaxed continuous min-cut problem (A.3). But in numerics, the continuous max-flow formulation (A.4) presents a linear programming subject to some simple convex constraints ((A.5) and (A.6)) joint with a linear equality constraint (A.7), which is much simpler than the convex relaxed continuous min-cut problem (A.3) considering the non-smooth total-variation function in (A.3); moreover, Yuan et al. (2010a, 2013) introduced an efficient algorithm to the convex relaxed continuous min-cut problem (A.3) based on the continuous max-flow formulation (A.4) and the modern augmented Lagrangian algorithm (see Yuan et al. (2010a, 2013) for details).

Comparing to the classical max-flow algorithm over the spatially discrete graph, the continuous max-flow algorithm can be easily implemented in the modern parallel computing platform (e.g. GPU), which greatly improves its computational efficiency. The basic implementations on Matlab, both CPU and GPU versions, are publicly available.¹

Appendix B. Proof of Proposition 1

Proof. The proof utilizes the primal and dual theory of convex optimization (Bertsekas, 1982). We list the main analytical steps as follows, and refer to Yuan et al. (2010a,b) for analysis details.

Introduce the multiplier functions $u_i(x)$, $i \in WG \cup L$, to each respective flow residue functions $G_i(x)$ defined in the flow conservation constraints (12) and (13). We can then express the *continuous max-flow formulation* (9) equivalently as follows:

$$\min_u \max_{p,q} L(u; p, q) := \int_{\Omega} p_o(x)dx + \sum_{i \in WG \cup L} \langle u_i, G_i \rangle, \quad (\text{B.1})$$

subject to the flow capacity constraints (10) and (11). Clearly, the energy function $L(u; p, q)$ of (B.1) just gives the Lagrangian function of the constrained maximization problem (9).

For the minimax optimization problem (B.1), given its linear energy function and convex constraints, the min and max operations are interchangeable (Ekeland and Témam, 1999), such that

$$\min_u \max_{p,q} L(u; p, q) = \max_{p,q} \min_u L(u; p, q).$$

Therefore, to compute the saddle point of (B.1), we first maximize (B.1) over the sink flows $p_i(x)$, $i \in L$, subject to (10), which gives rise to

$$u_i(x) \geq 0, \quad i \in L;$$

¹ <http://www.mathworks.com/matlabcentral/fileexchange/authors/206616>.

then maximize (B.1) over the two free flows $p_o(x)$ and $p_{WG}(x)$, which results in

$$u_{WG}(x) + u_B(x) = 1, \quad u_{WG}(x) - (u_{CG} + u_{PZ})(x) = 0;$$

and maximize (B.1) over the spatial flows $q_i(x)$, $i \in WG \cup L$, subject to (12), which directly amounts to the sum of the weighted total variation functions of $u_i(x)$, $i \in WG \cup L$. Through simple computation and reorganization, then the *convex relaxed optimization model* (8) follows.

Therefore, we have

$$(9) \iff (B.1) \iff (8).$$

Proposition 1 is proved. \square

Appendix C. Duality-based optimization algorithm

As shown in Appendix B, the primal–dual optimization problem (B.1) is equivalent to the *continuous max-flow model* (9), where the labeling functions $u_i(x)$, $i \in WG \cup L$, work as the multipliers to the respective linear equality constraints (12) and (13) of flow conservation. In addition, the energy function of (B.1) is just the associated Lagrangian function of the flow-maximization problem (9) constrained by flow conservation conditions (12) and (13). Hence, an efficient *duality-based optimization algorithm* can be derived by the theory of augmented multiplier algorithms (Bertsekas, 1982), which iteratively optimizes the following augmented Lagrangian function:

$$\max_{p,q} \min_u L_c(u; p, q) := L(u; p, q) - \frac{c}{2} \sum_{i \in WG \cup L} \|G_i\|^2,$$

subject to the flow capacity constraints (10) and (11), where $L(u; p, q)$ is the Lagrangian function (B.1) associated with the *continuous max-flow model* (9).

The proposed *duality-based optimization algorithm* explores the following steps at each k -th iteration:

- Maximize $L_c(u; p, q)$ over the spatial flows $|q_i(x)| \leq g(x)$, $i \in WG \cup L$, while fixing the other variables of $(u; p)^k$, which amounts to

$$q_i^{k+1} := \arg \max_{|q_i(x)| \leq g(x)} -\frac{c}{2} \left\| \operatorname{div} q_i - F_i^k \right\|^2, \quad (C.1)$$

where $F_i^k(x)$, $i \in WG \cup L$, is directly computed by the fixed variables of u and q . This can be computed by the gradient-projection iteration:

$$q_i^{k+1} = \operatorname{Proj}_{|q_i(x)| \leq g(x)} (q_i^k + \tau \nabla (\operatorname{div} q_i^k - F_i^k)); \quad (C.2)$$

where $\tau > 0$ is the step-size for convergence (Chambolle, 2004).

- Maximize $L_c(u; p, q)$ over the free source flow $p_o(x)$, while fixing the other variables of $(u; p, q)^k$, which amounts to

$$(p_o)^{k+1} := \arg \max_{p_o} \int_{\Omega} p_o dx - \frac{c}{2} \sum_{i \in \{WG, B\}} \|p_o - J_i^k\|^2,$$

where $J_i^k(x)$, $i \in \{WG, B\}$, is directly computed by the fixed variables. This can be solved exactly by:

$$(p_o)^{k+1}(x) = (J_B^k(x) + J_C^k(x) + 1/c)/2. \quad (C.3)$$

- Maximize $L_c(u; p, q)$ over the free flow $p_{WG}(x)$, while fixing the other variables of $(u; p, q)^k$, which amounts to

$$(p_{WG})^{k+1} := \arg \max_{p_{WG}} -\frac{c}{2} \sum_{i \in \{WG, CG, PZ\}} \|p_{WG} - T_i^k\|^2,$$

where $T_i^k(x)$, $i \in \{WG, CG, PZ\}$, is directly computed by the fixed variables. This can be solved exactly by:

$$(p_{WG})^{k+1}(x) = \frac{1}{3} \sum_{i \in \{WG, CG, PZ\}} T_i^k(x). \quad (C.4)$$

- Maximize $L_c(u; p, q)$ over $p_i(x) \leq \rho_i(x)$, $i \in L$, while fixing the other variables of $(u; p, q)^k$, which amounts to

$$(p_i)^{k+1} := \arg \max_{p_i(x) \leq \rho_i(x)} -\frac{c}{2} \|p_i - H_i^k\|^2,$$

where $H_i^k(x)$, $i \in L$, is directly computed by the fixed variables. This can be solved exactly by:

$$(p_i)^{k+1}(x) = \min(H_i^k(x), \rho_i(x)). \quad (C.5)$$

- Update the labeling functions $u_i(x)$, where $i \in WG \cup L$, by

$$u_i^{k+1} = u_i^k - c G_i^k(x), \quad i \in WG \cup L \quad (C.6)$$

where $G_i^k(x)$, $i \in WG \cup L$, stands for the respective flow residue function.

The experiments show only one gradient-projection iteration (C.2) is required to achieve convergence, which greatly improves numerical efficiency. Clearly, the proposed *duality-based optimization algorithm* enjoys great numerical advantages in that it successfully avoids directly tackling non-smooth total-variation functions in the energy of the *convex relaxed optimization problem* (8) by the projections to the simple convex sets, and also implicitly implements the labeling constraints (5) and (6) by the introduced flow-maximization configuration (as illustrated in Fig. 6). Moreover, the *duality-based optimization algorithm* is implemented and computed in parallel and achieves a high numerical performance in practice.

References

- Allen, P., Graham, J., Williamson, D., Hutchinson, C., 2006. Differential segmentation of the prostate in MR images using combined 3d shape modelling and voxel classification. In: 3rd IEEE International Symposium on Biomedical Imaging: Nano to Macro, 2006. IEEE, pp. 410–413.
- Bertsekas, D.P., 1982. Constrained optimization and Lagrange multiplier methods. In: Computer Science and Applied Mathematics. Academic Press Inc., New York.
- Beyersdorff, D., Winkel, A., Hamm, B., Lenk, S., Loening, S.A., Taupitz, M., 2005. MR imaging-guided prostate biopsy with a closed MR unit at 1.5 T: initial results. *Radiology* 234, 576–581.
- Boykov, Y., Jolly, M.P., 2001. Interactive graph cuts for optimal boundary and region segmentation of objects in n-d images, in: Proceedings. Eighth IEEE International Conference on Computer Vision, 2001. ICCV 2001, pp. 105–112.
- Boykov, Y., Veksler, O., Zabih, R., 2001. Fast approximate energy minimization via graph cuts. *IEEE Trans. Pattern Anal. Mach. Intell.* 23, 2001.
- Chambolle, A., 2004. An algorithm for total variation minimization and applications. *J. Math. Imag. Vision* 20, 89–97.
- Chan, T.F., Vese, L.A., 2001. Active contours without edges. *IEEE Trans. Imag. Process.* 10, 266–277.
- Chan, T.F., Esedoglu, S., Nikolova, M., 2006. Algorithms for finding global minimizers of image segmentation and denoising models. *SI AM J. Appl. Math.* 66, 1632–1648 (electronic).
- Delong, A., Gorelick, L., Schmidt, F., Veksler, O., Boykov, Y., 2011. Interactive segmentation with super-labels. In: EMMCVPR, pp. 147–162.
- Ding, M., Chiu, B., Gyacskov, I., Yuan, X., Drangova, M., Downey, D.B., Fenster, A., 2007. Fast prostate segmentation in 3D TRUS images based on continuity constraint using an autoregressive model. *Med. Phys.* 34, 4109–4125.
- Doyle, S., Feldman, M.D., Tomaszewski, J., Madabhushi, A., 2012. A boosted bayesian multiresolution classifier for prostate cancer detection from digitized needle biopsies. *IEEE Trans. Biomed. Eng.* 59, 1205–1218.
- Ekeland, I., Témam, R., 1999. Convex Analysis and Variational Problems. Society for Industrial and Applied Mathematics, Philadelphia, PA, USA.
- Gao, Y., Sandhu, R., Fichtinger, G., Tannenbaum, A., 2010. A coupled global registration and segmentation framework with application to magnetic resonance prostate imagery. *IEEE Trans. Med. Imag.* 29, 1781–1794.
- Garnier, C., Bellanger, J.J., Wu, K., Shu, H., Costet, N., Mathieu, R., de Crevoisier, R., Coatrieux, J.L., 2011. Prostate segmentation in HIFU therapy. *IEEE Trans. Med. Imag.* 30, 792–803.
- Ghose, S., Oliver, A., Martí, R., Lladó, X., Vilanova, J., Freixenet, J., Mitra, J., Sidibé, D., Meriaudeau, F., 2012. A survey of prostate segmentation methodologies in ultrasound, magnetic resonance and computed tomography images. *Comput. Methods Programs Biomed.* 108, 262–287.

- Haffner, J., Potiron, E., Bouyé, S., Puech, P., Leroy, X., Lemaitre, L., Villers, A., 2009. Peripheral zone prostate cancers: location and intraprostatic patterns of spread at histopathology. *Prostate* 69, 276–282.
- Hu, N., Downey, D.B., Fenster, A., Ladak, H.M., 2003. Prostate boundary segmentation from 3D ultrasound images. *Med. Phys.* 30, 1648–1659.
- Kass, M., Witkin, A., Terzopoulos, D., 1988. Snakes: active contour models. *Int. J. Comput. Vision* 1, 321–331.
- Khalvati, F., Salmanpour, A., Rahnamayan, S., Rodrigues, G., Tizhoosh, H.R., 2013. Inter-slice bidirectional registration-based segmentation of the prostate gland in MR and ct image sequences. *Med. Phys.* 40, 123503.
- Kirby, R., Gilling, P., 2011. *Fast Facts: Benign Prostatic Hyperplasia*. Health Press Limited.
- Klein, S., van der Heide, U.A., Raaymakers, B.W., Kotte, A.N., Staring, M., Pluim, J.P., 2007. Segmentation of the prostate in MR images by atlas matching. In: 4th IEEE International Symposium on Biomedical Imaging: From Nano to Macro, 2007. ISBI 2007. IEEE, pp. 1300–1303.
- Klein, S., van der Heide, U.A., Lips, I.M., van Vulpen, M., Staring, M., Pluim, J.P., 2008. Automatic segmentation of the prostate in 3d MR images by atlas matching using localized mutual information. *Med. Phys.* 35, 1407–1418.
- Kolmogorov, V., Zabih, R., 2004. What energy functions can be minimized via graph cuts. *IEEE Trans. Pattern Anal. Mach. Intell.* 26, 65–81.
- Langerak, T.R., van der Heide, U.A., Kotte, A.N., Viergever, M.A., van Vulpen, M., Pluim, J.P., 2010. Label fusion in atlas-based segmentation using a selective and iterative method for performance level estimation (SIMPLE). *IEEE Trans. Med. Imag.* 29, 2000–2008.
- Lellmann, J., Kappes, J.H., Yuan, J., Becker, F., Schnörr, C., 2009. Convex multi-class image labeling by simplex-constrained total variation. In: SSVI, pp. 150–162.
- Leslie, S., Goh, A., Lewandowski, P.M., Huang, E.Y.H., de Castro Abreu, A.L., Berger, A.K., Ahmadi, H., Jayaratna, I., Shoji, S., Gill, I.S., Ukimura, O., 2012. 2050 contemporary image-guided targeted prostate biopsy better characterizes cancer volume, Gleason grade and its 3d location compared to systematic biopsy. *J. Urol.* 187, e827.
- Li, W., Liao, S., Feng, Q., Chen, W., Shen, D., 2012. Learning image context for segmentation of the prostate in ct-guided radiotherapy. *Phys. Med. Biol.* 57, 1283.
- Litjens, G., Debats, O., van de Ven, W., Karssemeijer, N., Huisman, H., 2012. A pattern recognition approach to zonal segmentation of the prostate on MRI. In: *Medical Image Computing and Computer-Assisted Intervention – MICCAI 2012*, pp. 413–420.
- Mahdavi, S.S., Moradi, M., Wen, X., Morris, W.J., Salcudean, S.E., 2011. Evaluation of visualization of the prostate gland in vibro-elastography images. *Med. Imag. Anal.* 15, 589–600.
- Makni, N., Iancu, A., Colot, O., Puech, P., Mordon, S., Betrouni, N., et al., 2011. Zonal segmentation of prostate using multispectral magnetic resonance images. *Med. Phys.* 38, 6093.
- Martin, S., Troczak, J., Daanen, V., 2010. Automated segmentation of the prostate in 3D MR images using a probabilistic atlas and a spatially constrained deformable model. *Med. Phys.* 37, 1579.
- Mazaheri, Y., Hricak, H., Fine, S.W., Akin, O., Shukla-Dave, A., Ishill, N.M., Moskowitz, C.S., Grater, J.E., Reuter, V.E., Zakian, K.L., et al., 2009. Prostate tumor volume measurement with combined t2-weighted imaging and diffusion-weighted MR: correlation with pathologic tumor volume. *Radiology* 252, 449–457.
- McNeal, J.E., 1981. The zonal anatomy of the prostate. *Prostate* 2, 35–49.
- MICCAI, 2012. *Grand Challenge: Prostate MR Image Segmentation*.
- Niaf, E., Rouvière, O., Mège-Lechevallier, F., Bratan, F., Lartizien, C., 2012. Computer-aided diagnosis of prostate cancer in the peripheral zone using multiparametric MRI. *Phys. Med. Biol.* 57, 3833.
- Qiu, W., Yuan, J., Ukwatta, E., Tessier, D., Fenster, A., 2012. Rotational-slice-based prostate segmentation using level set with shape constraint for 3D end-firing TRUS guided biopsy. In: *MICCAI (Part 1)*, LNCS, vol. 7510, pp. 536–543.
- Qiu, W., Yuan, J., Kishimoto, J., Ukwatta, E., Fenster, A., 2013a. Lateral ventricle segmentation of 3d pre-term neonates us using convex optimization. In: *Medical Image Computing and Computer-Assisted Intervention–MICCAI 2013*. Springer, Berlin Heidelberg, pp. 559–566.
- Qiu, W., Yuan, J., Ukwatta, E., Rajchl, M., Sun, Y., Fenster, A., 2013b. Efficient 3d multi-region prostate MRI segmentation using dual optimization. In: *Information Processing in Medical Imaging (IPMI)*.
- Qiu, W., Yuan, J., Ukwatta, E., Sun, Y., Rajchl, M., Fenster, A., 2013c. Fast globally optimal segmentation of 3d prostate MRI with axial symmetry prior. In: *Medical Image Computing and Computer-Assisted Intervention–MICCAI 2013*. Springer, Berlin Heidelberg, pp. 198–205.
- Qiu, W., Yuan, J., Ukwatta, E., Tessier, D., Fenster, A., 2013d. 3D prostate segmentation using level set with shape constraint based on rotational slices for 3D end-firing TRUS guided biopsy. *Med. Phys.* 40.
- Qiu, W., Yuchi, M., Ding, M., Tessier, D., Fenster, A., 2013e. Needle segmentation using 3D hough transform in 3D TRUS guided prostate transperineal therapy. *Med. Phys.* 40, 042902-1–042902-13.
- Siegel, R., Naishadham, D., Jemal, A., 2012. *Cancer statistics, 2012*. CA: A Cancer J. Clin. 62, 10–29.
- Smith, W.L., Lewis, C., Bauman, G., Rodrigues, G., DSouza, D., Ash, R., Ho, D., Venkatesan, V., Downey, D., Fenster, A., 2007. Prostate volume contouring: A 3D analysis of segmentation using 3D TRUS, CT, and MR. *Int. J. Radiat. Oncol. Biol. Phys.* 67, 1238–1247.
- Sonn, G.A., Natarajan, S., Margolis, D.J., MacAiran, M., Lieu, P., Huang, J., Dorey, F.J., Marks, L.S., 2013. Targeted biopsy in the detection of prostate cancer using an office based magnetic resonance ultrasound fusion device. *J. Urol.* 189, 86–92.
- Toth, R., Ribault, J., Gentile, J., Sperling, D., Madabhushi, A., 2013. Simultaneous segmentation of prostatic zones using active appearance models with multiple coupled levelsets. *Comput. Vision Image Understand.* 1051–1060.
- Ukwatta, E., Yuan, J., Rajchl, M., Qiu, W., Tessier, D., Fenster, A., 2013. 3d carotid multi-region MRI segmentation by globally optimal evolution of coupled surfaces. *IEEE Trans. Med. Imag.* 32, 770–785.
- Villeirs, G., De Meerleer, G., 2007. Magnetic resonance imaging (MRI) anatomy of the prostate and application of MRI in radiotherapy planning. *Eur. J. Radiol.* 63, 361–368.
- Vincent, G., Guillard, G., Bowes, M., 2012. Fully automatic segmentation of the prostate using active appearance models. In: *MICCAI Challenge: Prostate MR Segmentation*.
- Wang, H., Suh, J., Das, S., Pluta, J., Craige, C., Yushkevich, P., 2013. Multi-atlas segmentation with joint label fusion. *IEEE Trans. Pattern Anal. Mach. Intell.* 35, 611–623.
- Xue, H., Srinivasan, L., Jiang, S., Rutherford, M., Edwards, A.D., Rueckert, D., Hajnal, J.V., 2007. Automatic segmentation and reconstruction of the cortex from neonatal MRI. *Neuroimage* 38, 461–477.
- Yin, Y., Fotin, S., Periaswamy, S., Kunz, J., Haldankar, H., Muradyan, N., Turkbey, B., Choyke, P., 2012. Fully automated 3d prostate central gland segmentation in mr images: a logismos based approach. In: *SPIE Medical Imaging, International Society for Optics and Photonics*, pp. 83143B–83143B.
- Yuan, J., Bae, E., Tai, X., 2010a. A study on continuous max-flow and min-cut approaches. In: *CVPR*.
- Yuan, J., Bae, E., Tai, X.C., Boykov, Y., 2010b. A continuous max-flow approach to potts model. In: *ECCV*.
- Yuan, J., Qiu, W., Ukwatta, E., Rajchl, M., Sun, Y., Fenster, A., 2012. An efficient convex optimization approach to 3D prostate MRI segmentation with generic star shape prior. In: *Prostate MR Image Segmentation Challenge, MICCAI*.
- Yuan, J., Bae, E., Tai, X.C., Boykov, Y., 2013. A spatially continuous max-flow and min-cut framework for binary labeling problems. *Numer. Math.* 1, 1–29.
- Zijdenbos, A.P., Dawant, B.M., Margolin, R.A., Palmer, A.C., 1994. Morphometric analysis of white matter lesions in MR images: method and validation. *IEEE Trans. Med. Imag.* 13, 716–724.
- Zou, K.H., Mcdermott, M.P., 1999. Higher-moment approaches to approximate interval estimation for a certain intraclass correlation coefficient. *Stat. Med.* 18, 2051–2061.